ADVANCED MATERIALS INTERFACES
www.advmatinterfaces.de

Self-Assembly of Colloidal Nanoparticles into Well-Ordered Centimeter-Long Rods via Crack Engineering

Jingli Xie, Junchang Guo, Dehui Wang, Yu Cang, Wenluan Zhang, Jiajia Zhou, Bo Peng, Yanbo Li, Jiaxi Cui, Longquan Chen, George Fytas, and Xu Deng**

Self-assembly of colloidal nanoparticles (NPs) is widely employed in nanofabrication to have regulated shape with fascinating functions. However, to have a specific desired shape at centimeter-scale without template is challenging. Herein, by harnessing the colloidal nanoparticle thin film crack engineering, robust and highly transparent centimeter-scale rods with uniform width and thickness are obtained. The dimension of these rods can be tailored via controlling the solvent composition, NPs volume fraction, and suspension descending rate. Their mechanical stiffness and elastic properties can be further improved by thermal annealing. It is demonstrated that these rods can be used as probes for surface enhanced Raman scattering detection making use of their rich nanostructured surface. This crack engineering strategy can be used as a universal method to assemble the nanoscale colloids into centimeter-scale rods for analytical and photoelectrical applications.

In the field of nanofabrication, to have regulated shape of a large number of colloidal nanoparticles (NPs), self-assembly usually plays an essential role.[1] Through self-assembly, a variety of regulated shapes, e.g., Janus sphere, membrane, strip, and rod, which are all created from colloidal NPs attract broad interests.[2–4] For example, this nanofabrication strategy can be utilized to obtain photonic crystals composed of NPs that respond to mechanical stress like fingerprinting.[5] It can also be employed in forming 3D template to fabricate large inverse opal that exhibits gas adsorption properties.[6] Among all these shapes, colloidal rods (CRs) catch people's eyes in diverse applications such as photonic devices,[7] battery electrodes,[8] surface patterning,[9] etc. However, due to the weak interaction between NPs in the assembling process, the resulted rods are usually in the length scale of micrometer.[10–12] Obtaining CRs of centimeter-long is still challenging. To tackle this issue, the most common method is to use specific template. However, the use of templates demands delicate operating conditions and results into high manufacturing cost.[10,13,14] Hence, to assemble colloidal NPs into uniform centimeter-scale shape in a facile template-free manner is in great need.

In this work, we report a unique strategy to assemble colloidal NPs into uniform centimeter-scale CRs by harnessing the crack engineering without any templates. Due to tensile stress, cracks are often observed in a wet film where NPs of the suspension self-assemble into some specific shapes via drying. In general, cracks are undesirable and regarded as a negative factor in numerous applications.[15,16] Therefore, most of previous efforts were devoted to circumventing them.[15,17,18] Recently, it has been demonstrated that regulated crack patterns could be useful in some applications, such as fabrication of microchannels,[9,19] photonic microbricks,[20] and sensors,[21] due to their excellent controllability of morphology and periodicity. Herein, we utilized rational designed cracks to obtain uniform CRs. Their dimension can be tailored by adjusting solvent composition, suspension descending rate, and NPs volume fraction. The mechanical stiffness of rods is reinforced by annealing without significantly altering the surface nanostructure. Therefore, this strategy is potentially scalable and applicable for numerous types of nanoparticle with multifunctional properties. The resulted CRs' nanostructured surface and the controllable dimension make these CRs appealing for many practical applications.

We started with radial directional crack pattern. When a droplet of colloidal suspension is dribbled onto a substrate, cracks form and propagate radially inward as solvent evaporates (**Figure 1**a). The evaporation process is illustrated in Figure S1a

J. Xie, J. Guo, D. Wang, Dr. W. Zhang, Prof. Y. Li, Prof. J. Cui, Prof. X. Deng
Institute of Fundamental and Frontier Sciences
University of Electronic Science and Technology of China
Chengdu 610054, China
E-mail: wenluanzh@uestc.edu.cn; dengxu@uestc.edu.cn
Dr. Y. Cang, Prof. G. Fytas
Max Planck Institute for Polymer Research
Ackermannweg 10, Mainz 55128, Germany
Dr. W. Zhang
School of Automation Engineering
University of Electronic Science and Technology of China
Chengdu 611731, China
Prof. J. Zhou
Center of Soft Matter Physics and Its Application
Beihang University
Beijing 100191, China
Prof. B. Peng
School of Electronic Science and Engineering
University of Electronic Science and Technology of China
Chengdu 610054, China
Prof. L. Chen
School of Physics
University of Electronic Science and Technology of China
Chengdu 610054, China
The ORCID identification number(s) for the author(s) of this article can be found under https://doi.org/10.1002/admi.202000222.

DOI: 10.1002/admi.202000222

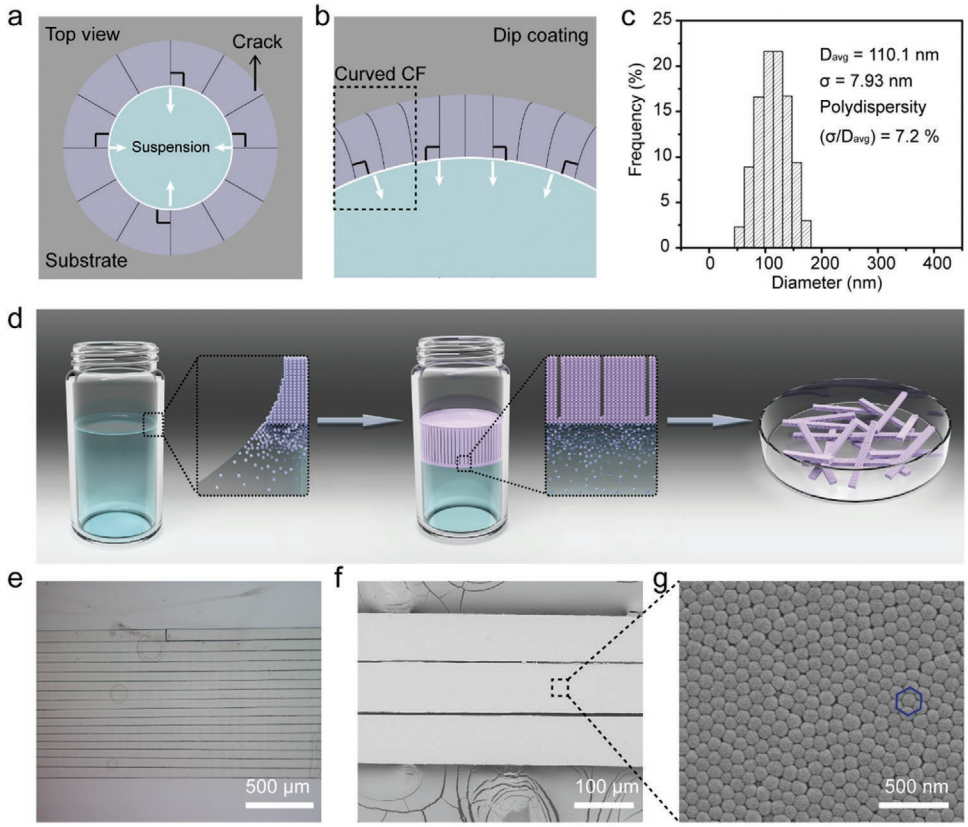

Figure 1. Strategy designed for uniform crack-induced CRs. a) Illustration of radial-directional crack pattern by sessile drop evaporation. The white line and arrows represent the compacting front and the evaporation direction, respectively. b) Illustration of feather-like crack pattern through dip-coating. c) Illustration of the meniscus on the substrate, h represents the meniscus height, and $h_1 > h_2$. d) Schematic drawing illustrating the preparation of the CRs. e) An optical image of crack-induced rods. f,g) SEM images of CRs at different magnification. The blue pattern shows that particles deposited in a hexagonal-like structure.

(Supporting Information). The evolution of crack propagation can be readily observed by means of optical microscopy (Movie S1, Supporting Information). A snapshot of Movie S1 (Supporting Information) is displayed in Figure S1b (Supporting Information), showing a full view of the entire crack pattern after complete evaporation of the solvent. After solvent drying, a rod consisting of colloidal NPs appears between two adjacent cracks. Since the crack propagates into the droplet center, the perimeter of compacting front (CF) becomes small as the solvent evaporates. Thus, the colloidal NPs form smaller rod end near the droplet center than the one away the center.[22] (For detailed illustration, please see Figure S2, Supporting Information.) To have rods with uniform width, we turned to feather-like crack pattern, which is usually observed during dip-coating. While pulling a substrate upward from a colloidal suspension, straight crack pattern appears in the central part of this substrate. The meniscus height in the central part of the substrate, h_1, can be expressed as:[23] $h_1 = \sqrt{2}\,\kappa^{-1}(1-\sin\theta)^{1/2}$, κ^{-1} is the capillary length, and θ is the water contact angle. This equation works only if the substrate is flat and the curvature radius is infinite. However, close to the substrate edge, the curvature increases substantially, the meniscus height near the substrate edge, h_2, can be written as:[23] $h_2 \sim b\ln(2\kappa^{-1}b^{-1})$, here, curvatures are of the order of b^{-1}. Thus, due to the increased curvature, the meniscus height decreases near the substrate edge and $h_1 > h_2$. This difference in menicus height then leads to curved compacting front. Since the crack propagation direction is vertical to the compacting front, the generated cracks thus bend accordingly, thus rendering curved rods. This phenomenon is illustrated in Figure 1b and Figure S1d (Supporting Information). Therefore, to obtain completely straight rods, we used small vial for generating cracks, which has no boundary effect when solvent evaporates along the vertical direction, because the cracks arrange in a close-loop at the horizontal level.

Indeed, by adjusting crack patterns, we managed to have uniform centimeter-scale CRs. A vial with colloidal suspension containing 110 nm diameter monodispersed SiO_2 NPs (Figure S3, Supporting Information) was placed in an oven with temperature ranging from 50 to 90 °C. As solvent evaporated, silica NPs accumulated at the three-phase contact line and were adsorbed on the vial's wall. Then, cracks appeared and propagated gradually to form CRs (Figure 1d). After the liquid level decreased by 1 cm, residue suspension was removed and the resulted rods were left alone for half an hour to be completely dried. In this work, we used 10 cm high vials for all the CRs fabrication. Hence, the silica NPs volume fraction does not change significantly during the solvent evaporation, so that we were able to obtain 1 cm long CRs with uniform thickness, width, and good reproducibility, as shown in Figure 1e and Figure S4 (Supporting Information). High-magnification image

from scanning electron microscope (SEM) (Figure 1g) proves that these rods are entirely composed of hexagonal-like arrangements. In the drying process, solvent evaporation causes NPs aggregate into close-packed structure, binding to the substrate and generating transverse tensile stress.[24,25] Once the tensile stress exceeds a critical value, cracks occur and propagate along the solvent retreating direction. Since the edge of cracks are very sharp, the resulted rods are very neat and without any serration in the side (Figure S5, Supporting Information).

In previous works, dip-coating was usually applied to construct various colloid patterns, and pure water was used as solvent.[21] However, by evaporating colloidal suspension using water as solvent, we cannot obtain uniform thin film composed of silica NPs, not mentioning CRs. It is possible that, unlike the nonequilibrium dynamic process happens during dip-coating, the spontaneous evaporation of water is pretty slow resulting into a quasi-equilibrium state of the colloidal suspension, which cannot confine the NPs aggregation to the vial's wall to form uniform thin film. In practice, we added ethanol into water to enhance the solvent evaporation rate. But this mixture of water and ethanol rendered tears of wine phenomenon, a classic Marangoni effect, with ethanol concentration up to 80 vol%, as shown in Figure S6 and Movie S2 (Supporting Information).[26] Small droplets were dragged by gravity downwards back to the suspension disrupting the formation of colloidal film. Thus, only small amount of NPs were deposited in the film, which was not thick enough to induce cracks, as shown in Figure S6 (Supporting Information). When the ethanol concentration higher is than 90 vol%, colloidal film can grow thick and uniform CRs were finally obtained. High concentration ethanol/water suspension was prepared via dialysis, which required ultralarge amount of ethanol to get 99 vol% concentration. In practice, 90 vol% ethanol suspension could render uniform CRs, which was not improved significantly by using 99 vol% ethanol suspension. Thus, we sticked to the 90 vol% ethanol suspension for the rest of the work.

To get desired CRs dimension, like rod thickness (H) and width (W), we studied the effect of silica NPs volume fraction and suspension descending rate. By keeping suspension descending rate 1 μm s^{-1} as constant, as shown in **Figure 2**a, H and W values increase linearly as the NPs volume fraction goes higher, reach about 70 μm and 160 μm, respectively. This is qualitatively natural because NPs volume fraction is closely related to particle flux. The particle flux, j_P, can be expressed as:[27] $j_P = N_P V_P v_P$, where N_P is the number of particles per unit volume, V_P is the volume of a single particle, and v_P is the mean velocity of the suspended particles. When NPs volume fraction, N_P goes higher, particle flux increases, driving more particles to evaporation region, thus rods get thicker and wider. Then, NPs volume fraction of 1.2 vol% was kept unchanged to study how suspension descending rate affected the CRs' dimension. Figure 2b shows that H and W values gradually decrease as the suspension evaporating faster, down to about 30 μm and 70 μm, respectively. The variation of rods' thickness is opposite to the

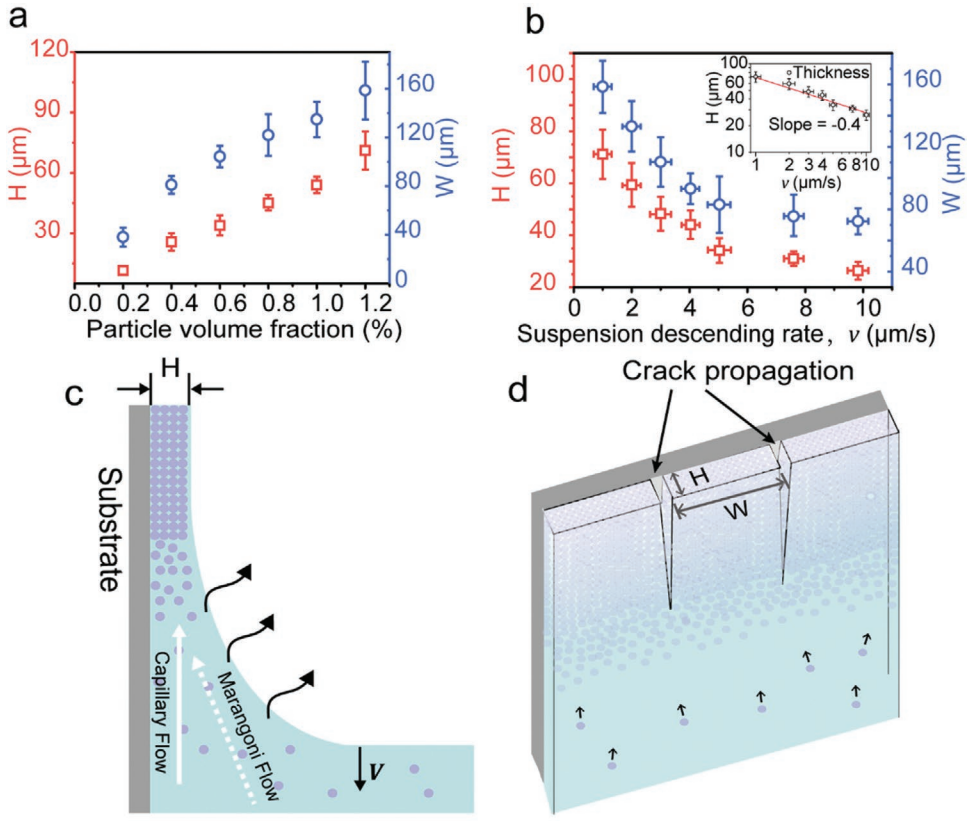

Figure 2. Experimental results of CRs dimension. a) Rods' width and thickness as a function of NPs volume fraction. b) The dependence of both rods width and thickness on the suspension descending rate. The inset is plotted in log–log scale. c) Flow pattern sketch of the drying suspension near the contact line. d) Schematic illustrating crack propagation during the deposition of NPs leading to the formation of rods.

variation trend of suspension descending rate, which is consistent with previous research.[27] The particle deposition time is directly related to suspension descending rate. The higher suspension descending rate will make the particle deposition time shorter, thus fewer particles are deposited in the evaporation region and the rods become thinner. The W values are in the same trend as the H values, which is in good agreement with previous study.[28] In this case, the suspension descending rate was controlled by heating temperature, obtaining beyond 10 μm s^{-1} is simply not possible because it would boil the ethanol/water mixture.

To get deeper understanding of the film formation mechanism and its correlated fluid mechanical properties, we propose the CRs formation mechanism in schematic graphs, shown in Figure 2c,d, and perform a qualitative analysis. Based on previous study on meniscus-guided coating,[29,30] we argue that the film deposition, in this case, is in the so-called "evaporative regime," since the capillarity and evaporation of the solvent dominate the wet film formation, NPs transport, and film solidification afterward. Normally, in this regime, dry film thickness is proportional to the suspension descending rate at the power of −1. However, in the inset of Figure 2b, the thickness (H) decreases by a power-law exponent of −0.4, which is larger than −1. Note that the previous power-law dependence of film thickness was derived by mass conservation law and neglecting flow recirculation induced by thermal Marangoni effect. In this study, the suspension descending rate is even lower than the lowest speed of the previous works. It is very possible that Marangoni flow contributes the thicker films as predicted by previous "evaporative regime" model. However, considering the complexity of fluid field, concentration, and temperature gradient induced by evaporation, it is still not feasible to give accurate model for the time being. Further investigation is needed in this interesting direction.

The CRs are composed of close-packed 110 nm NPs and the voids between NPs are much smaller than the wavelength of visible light, generating a highly transparent film, as verified by the ultraviolet–visible transmittance spectra (**Figure 3**a). However, these rods constructed by silica NPs are fragile and easily broken into pieces, making it difficult to be transferred. Hence, it is crucial to enhance the mechanical stiffness of the rods for practical application. According to a previous study,[31] the mechanical stiffness of the rods can be enhanced through annealing. Hence, we evaluated the effect of annealing temperature on rod morphology ranging from 800 to 1100 °C (Figure S9, Supporting Information). As the temperature was higher than 1000 °C, the silica NPs undergo high temperature deformation, resulting in the necking between NPs that gradually fused or fully sintered and the rod morphology changes. Under the premise of not changing the rod morphology, 900 °C was chosen as the annealing temperature. Annealing duration, on the other hand, plays an important role in improving the mechanical strength of rods due to the positive correlation between the annealing duration and the interactive force between silica NPs. For the untreated sample with the density of 1.69 kg cm^{-3}, the Young's (E) and shear (G) modulus determined by Brillouin light spectroscopy (BLS)[32] are 4.2 GPa and 1.8 GPa, respectively. As the annealing duration increases from 0.5 to 4 h, the rod density increases by 5%, from 2.13 to 2.24 kg cm^{-3}. Both E and G moduli are enhanced by about 250%, from 17.6 to 43.5 GPa, and from 8.2 to 19.1 GPa, respectively (Figure 3b). This extreme increase of the elasticity is attributed mainly to the huge packing (density) effect but also to the increased elasticity of the NPs due to size shrinking with annealing (Figure S10, Supporting Information). Notably the Poisson's ratio ($\nu = 0.1$) of CRs annealed for 0.5 h is lower than in the amorphous glass ($\nu = 0.16$).

For practical application, these highly uniform nanostructured CRs can be employed as probes for surface enhanced Raman scattering (SERS) detection. SERS, as a signal amplification and detection technique, has shown great potential for imaging and sensing applications.[33,34] Accordingly, a variety of efficient plasmonic nanostructures have been fabricated to achieve the SERS-based signal amplification and detection of trace molecules.[35,36] However, it remains a great challenge to transform the analytical sensitivity of SERS detection into a practical in situ diagnostic probe, mainly from the difficulty to prepare a robust, metal-coated SERS substrate. The enhancements occur at nanogaps between the neighboring metal nanostructure (hot spot); to obtain more nanogaps, the SERS

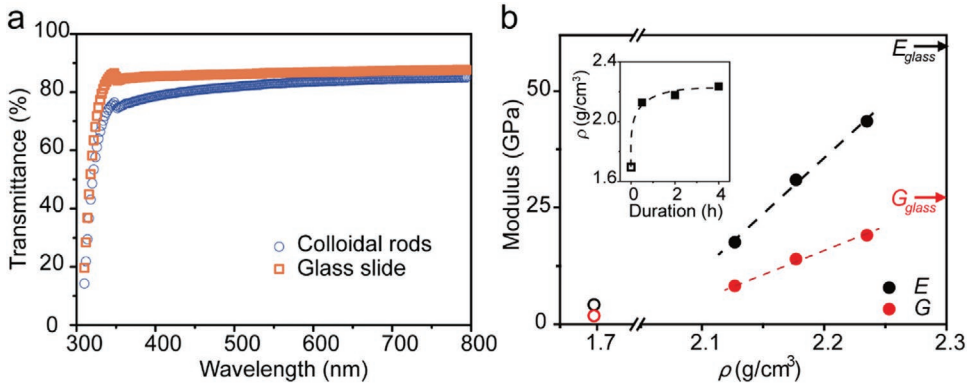

Figure 3. Optical transparency and mechanical stiffness of CRs. a) Ultraviolet–visible transmittance spectra of silica rods compared to glass slide. b) Young's modulus E and shear modulus G as a function of density of as-prepared (open symbols) and annealed (solid symbols) CRs. Inset: The density of CRs depends as a function of the annealing duration. The open square represents the density of as-prepared rods without annealing. For a comparison, the E and G of amorphous glass, assuming the density ρ = 2.3 g cm^{-3}, are denoted by black and red arrows, respectively. All the dashed lines in the figure are guides to the eye.

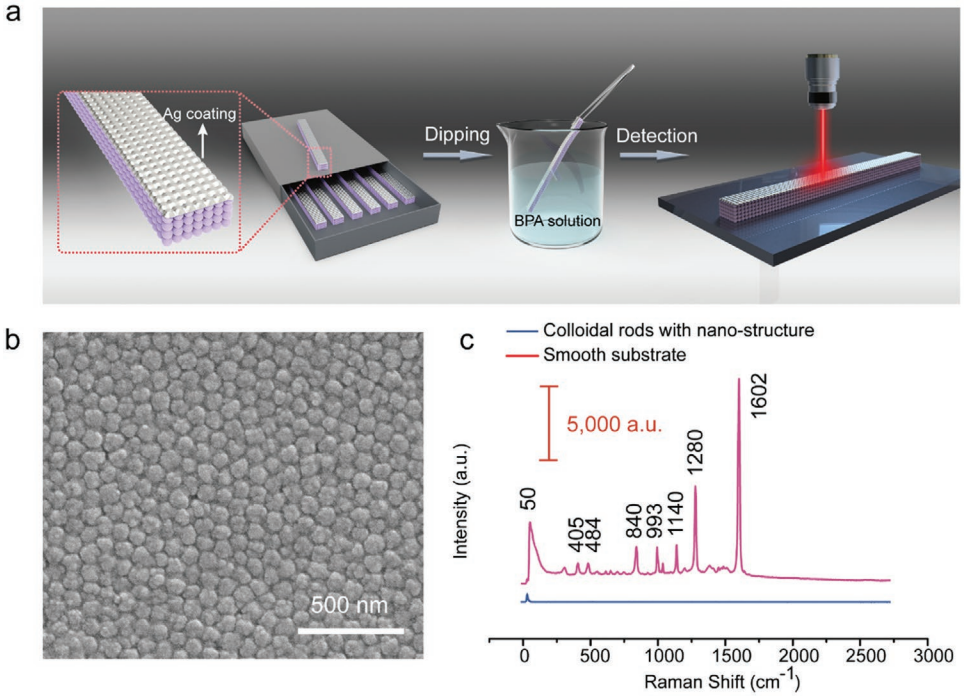

Figure 4. Effect of substrate structure on the SERS signal intensity. a) Schematic outlining the fabrication process of the Ag-coating nanostructured probe. b) SEM image of the Ag-coated nanostructured probe. c) SERS spectra obtained from 10^{-8} M BPA on different substrates.

substrate is required to process into a rough surface with nanostructure. In this study, CRs are composed of nanoparticles, providing a rough surface for SERS substrate and not requiring further processing, as shown in the atomic force microscopy (AFM) image in Figure S11 (Supporting Information). We utilized these CRs for SERS as a show case as shown in **Figure 4**a. Once the CRs were fabricated, they were coated with a thin (30 nm) silver layer through electron beam evaporation. After the deposition of silver layer, SEM analysis was performed (Figure 4b) to confirm that the origin of the observed SERS effects arose from the nanogap structure. Control substrates were also fabricated using above method where silica rod substrate was replaced by silicon wafers with a 300-nm-thick oxide layer, yielding a smooth unpatterned surface. We chose Bisphenol A (BPA) as target molecule, since its broad existence in plastic packages, and it is harmful to the endocrine system once released and entered human body. As shown in Figure 4c, SERS spectra of 10^{-8} M BPA adsorbed on these two substrates are recorded with laser excitation source of 633 nm wavelength. The spectra recorded using nanostructured substrate showed an obvious SERS response. The characteristic Raman peaks of BPA at 405, 484, 840, 993, 1140, 1280, and 1602 cm^{-1} can be observed. However, no appreciable Raman signal is observed from the control substrate (the blue spectra). Above results strongly support the fact that the nanostructured substrates are densely decorated by Ag, forming 3D plasmonic structure which provides abundant hot spots to have better SERS performance.

In summary, by controlling the stress distribution inside the colloidal film and crack formation during the evaporation of colloidal suspension, we successfully obtained centimeter-scale CRs with highly uniform width and thickness. The dimension of these CRs can be tailored by controlling NPs volume fraction and suspension descending rate. These colloid rods are transparent and the mechanical stiffness can be tuned by thermal annealing. For practical application, these robust rods can be used to fabricate probes in SERS detection. In addition to probes, these robust, regulated rods which could be manufactured in large scale may have potential values for a wide range of applications, including sensors, photonics, and lithography.

Experimental Section

Synthesis and Purification of Silica Nanoparticles: Colloidal suspension containing silica nanoparticles was prepared via a modified Stöber method by hydrolysis and condensation of TEOS (Sigma Aldrich) in ethanol (Aladdin), in presence of ammonia (TCI) as catalyst. First, a 250 mL flask containing 100 mL ethanol and 10 mL ammonia was stirred and heated to 60 °C. Then 6 mL TEOS were added and the mixture was kept under stirring for 8 h under 60 °C. Excess ammonia and unreacted reagents were removed by dialysis in deionized water.

Preparation of Uniform Microscale CRs: Glass vials (As-One) containing colloidal suspension were dried in an oven. Suspension descending rate was adjusted by changing oven's temperature, ranging from 50 to 100 °C. Once the suspension surface dropped for 1 cm, residual suspension was taken out and the sample was kept drying to completely remove the solvent. Uniform colloidal rods were peeled off by gently shaking the vials.

SERS Detection: For the SERS measurement of the analyte solution, the 10^{-8} M BPA solution was obtained by dissolving BPA in ethanol. 10 µL of this probe solution was dropped directly on the tested substrate and allowed to dry prior to measurement of the spectra. Then, these samples were totally dried for 10 min. The control substrates were purchased from Suzhou Research Materials Microtech Co., Ltd. All Raman

measurements were recorded using a confocal Raman microscope, which is coupled with a XY scanning stage (Laser wavelength at 633 nm, 0.52 mW laser power, 10 s acquisition time, etc.) These SERS spectra are completely the average spectra randomly collected from at least three points on each substrate.

Measurements and Characterizations: The NPs size measurements were performed at a Malvern Zetasizer Nano ZS instrument at 25 °C. The nanostructures of CRs were observed by field emission scanning electron microscope (FEI, INSPECT F) at an accelerating voltage of 20 kV and atomic force microscope (Bioscope Resolve, Brucker). The transmission was measured by an ultraviolet–visible spectrometer (UV-1900, Shimadzu Corporation). The sample for the above transmission measurement was also produced (Figure 1e).

BLS Experiment: The elasticities of CRs were determined by the noninvasive BLS technique. BLS detects the scattering of an incident probing beam from the thermally activated density fluctuations (phonons). The phonon wave vector, $\mathbf{q} = \mathbf{k_i} - \mathbf{k_s}$, is determined by the scattering geometry, where $\mathbf{k_i}$ and $\mathbf{k_s}$ are the incident and scattered photon wave vectors, respectively. The scattering wave vector $\mathbf{q}$ couples to the thermal phonons along the same direction with equal magnitude. The associated phonon energy is represented by the frequency shift $\pm\Delta f$ of inelastically scattered light resolved by an actively stabilized tandem FP interferometer (JRS Instruments). In this work, the transmission geometry was utilized to resolve the phonon propagation in the isotropic films. The phonon wave vector $q = 4\pi\sin\left(\frac{\theta}{2}\right)/\lambda$ in this geometry only depends on the scattering angle θ, where $\lambda = 532$ nm is the wavelength of the probing laser light. The acoustic longitudinal (L) and transverse (T) phonons are selectively recorded in the VV and VH spectra, respectively, where VV (VH) denotes a combination of vertical-polarized incident and vertical (horizontal)-polarized scattered light. The sound velocities of longitudinal (transverse) phonons are given by $c_{L(T)} = 2\pi\Delta f/q$. Then the elastic moduli E and G can be calculated from $E = \rho(3c_L^2 - 4c_T^2)/(c_L^2 - c_T^2)$ and $G = \rho c_T^2$ where ρ is the medium density. The typical VV and VH BLS spectra of CRs annealed for 0.5 h are shown in Figure S14 (Supporting Information).

Supporting Information

Supporting Information is available from the Wiley Online Library or from the author.

Acknowledgements

This work was supported by the National Natural Science Foundation of China (21603026). Y.C. and G.F. acknowledge the financial support by ERC AdG SmartPhon (Grant No. 694977).

Conflict of interest

The authors declare no conflict of interest.

Keywords

colloidal nanoparticles, cracks, self-assembly, solid–liquid interfaces, wettability

Received: February 10, 2020
Revised: June 22, 2020
Published online: August 2, 2020

[1] N. Vogel, M. Retsch, C. A. Fustin, A. del Campo, U. Jonas, *Chem. Rev.* **2015**, *115*, 6265.
[2] Q. Li, Y. Jia, L. R. Dai, Y. Yang, J. B. Li, *ACS Nano* **2015**, *9*, 2689.
[3] M. A. Boles, M. Engel, D. V. Talapin, *Chem. Rev.* **2016**, *116*, 11220.
[4] D. Mann, S. Voogt, H. Keul, M. Moller, M. Verheijen, P. Buskens, *Polymers* **2017**, *9*, 475.
[5] W. Cheng, Z. H. Han, Y. Du, J. Y. Qin, *Opt. Express* **2019**, *27*, 16071.
[6] T. S. Wang, B. Jiang, Q. Yu, X. Y. Kou, P. Sun, F. M. Liu, H. Y. Lu, X. Yan, G. Y. Lu, *ACS Appl. Mater. Interfaces* **2019**, *11*, 9600.
[7] J. W. Dong, X. D. Chen, H. Y. Zhu, Y. Wang, X. Zhang, *Nat. Mater.* **2017**, *16*, 298.
[8] J. H. Pikul, H. G. Zhang, J. Cho, P. V. Braun, W. P. King, *Nat. Commun.* **2013**, *4*, 1732.
[9] B. Li, B. B. Jiang, W. Han, M. He, X. Li, W. Wang, S. W. Hong, M. Byun, S. L. Lin, Z. Q. Lin, *Angew. Chem., Int. Ed.* **2017**, *56*, 4554.
[10] G. X. Wu, H. Cho, D. A. Wood, A. D. Dinsmore, S. Yang, *J. Am. Chem. Soc.* **2017**, *139*, 5095.
[11] L. X. Jiang, J. W. J. de Folter, J. B. Huang, A. P. Philipse, W. K. Kegel, A. V. Petukhov, *Angew. Chem., Int. Ed.* **2013**, *52*, 3364.
[12] B. Bharti, A. L. Fameau, M. Rubinstein, O. D. Velev, *Nat. Mater.* **2015**, *14*, 1104.
[13] Z. Rozynek, M. Han, F. Dutka, P. Garstecki, A. Jozefczak, E. Luijten, *Nat. Commun.* **2017**, *8*, 15255.
[14] N. Zhou, A. Zhang, L. Shi, K. Q. Zhang, *ACS Macro Lett.* **2013**, *2*, 116.
[15] J. L. Russell, G. H. Noel, J. M. Warren, N. L. L. Tran, T. E. Mallouk, *Langmuir* **2017**, *33*, 10366.
[16] B. Wang, A. L. Weldon, P. Kumnorkaew, B. Xu, J. F. Gilchrist, X. H. Cheng, *Langmuir* **2011**, *27*, 11229.
[17] K. R. Phillips, T. Shirman, E. Shirman, A. V. Shneidman, T. M. Kay, J. Aizenberg, *Adv. Mater.* **2018**, *30*, 1706329.
[18] W. Fan, M. Chen, S. Yang, L. M. Wu, *Sci. Rep.* **2015**, *5*, 12100.
[19] W. Han, B. Li, Z. Q. Lin, *ACS Nano* **2013**, *7*, 6079.
[20] K. R. Phillips, C. T. Zhang, T. Yang, T. Kay, C. Gao, S. Brandt, L. Liu, H. Z. Yang, Y. N. Li, J. Aizenberg, L. Li, *Adv. Funct. Mater.* **2020**, *30*, 1908242.
[21] O. Dalstein, E. Gkaniatsou, C. Sicard, O. Sel, H. Perrot, C. Serre, C. Boissiere, M. Faustini, *Angew. Chem., Int. Ed.* **2017**, *56*, 14011.
[22] G. Y. Jing, J. Ma, *J. Phys. Chem. B* **2012**, *116*, 6225.
[23] P.-G. De Gennes, F. Brochard-Wyart, D. Quéré, *Capillarity and Wetting Phenomena: Drops, Bubbles, Pearls, Waves*, Springer Science & Business Media, Berlin **2013**.
[24] R. Sengupta, M. S. Tirumkudulu, *Soft Matter* **2016**, *12*, 3149.
[25] N. Birk-Braun, K. Yunus, E. J. Rees, W. Schabel, A. F. Routh, *Phys. Rev. E* **2017**, *95*, 022610.
[26] J. B. Fournier, A. M. Cazabat, *Europhys. Lett.* **1992**, *20*, 517.
[27] B. G. Prevo, Y. Hwang, O. D. Velev, *Chem. Mater.* **2005**, *17*, 3642.
[28] M. I. Smith, J. S. Sharp, *Langmuir* **2011**, *27*, 8009.
[29] X. D. Gu, L. Shaw, K. Gu, M. F. Toney, Z. N. Bao, *Nat. Commun.* **2018**, *9*, 534.
[30] M. Faustini, B. Louis, P. A. Albouy, M. Kuemmel, D. Grosso, *J. Phys. Chem. C* **2010**, *114*, 7637.
[31] W. Widiyastuti, S. Y. Lee, F. Iskandar, K. Okuyama, *Adv. Powder Technol.* **2009**, *20*, 318.
[32] K. L. Kearns, T. Still, G. Fytas, M. D. Ediger, *Adv. Mater.* **2010**, *22*, 39.
[33] P. A. Mosier-Boss, *Nanomaterials* **2017**, *7*, 142.
[34] J. Lin, Y. Shang, X. X. Li, J. Yu, X. T. Wang, L. Guo, *Adv. Mater.* **2017**, *29*, 1604797.
[35] H. Kearns, R. Goodacre, L. E. Jamieson, D. Graham, K. Faulds, *Anal. Chem.* **2017**, *89*, 12666.
[36] Y. Huang, X. Zhang, J. H. Li, L. W. Ma, Z. J. Zhang, *J. Mater. Chem. C* **2017**, *5*, 6079.

ADVANCED MATERIALS INTERFACES

Supporting Information

for *Adv. Mater. Interfaces,* DOI: 10.1002/admi.202000222

Self-Assembly of Colloidal Nanoparticles into Well-Ordered Centimeter-Long Rods via Crack Engineering

Jingli Xie, Junchang Guo, Dehui Wang, Yu Cang, Wenluan Zhang, Jiajia Zhou, Bo Peng, Yanbo Li, Jiaxi Cui, Longquan Chen, George Fytas, and Xu Deng**

Supporting Information for

Self-assembly of colloidal nanoparticles into well-ordered centimeter-long rods via crack engineering

Jingli Xie, Junchang Guo, Dehui Wang, Yu Cang, Wenluan Zhang*, Jiajia Zhou, Bo Peng, Yanbo Li, Jiaxi Cui, Longquan Chen, George Fytas and Xu Deng*

Content

Supplementary Movie S1. The formation process of radial-directional crack patterns that observed by means of optical microscopy.

Supplementary Movie S2. The drying phenomenon under different ethanol concentration.

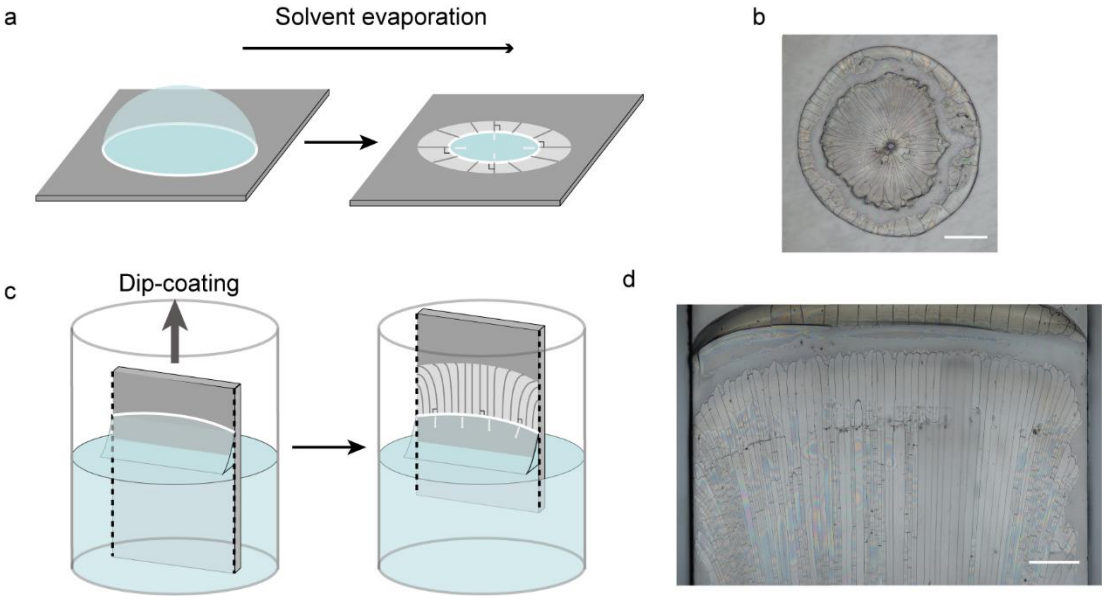

Figure S1. a) Schematic showing the forming process of radial-directional crack patterns. b) An optical microscope image of radial-directional crack patterns on glass substrate. c) Schematic showing the formation of feather-like crack patterns resulting in the curved solidification front near substrate boundary. d) An optical microscope

image of feather-like crack patterns on glass substrate through dip coating.

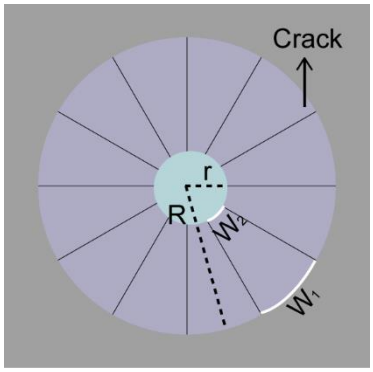

Figure S2. Suppose the initail suspension droplet radius is R, the number of cracks is N. When the droplet is complete dry, the compacting front stops moving with a inner circle's radius r. Thus, we can compare the length of rod's two ends, W_1 and W_2, by using compacting front's perimeter divided by crack number N. Hence, $\frac{W_1}{W_2} = \left(2\pi R/_N\right)/\left(2\pi r/_N\right) = \frac{R}{r}$. In general, R is much larger than r, so W_1 is larger than W_2.

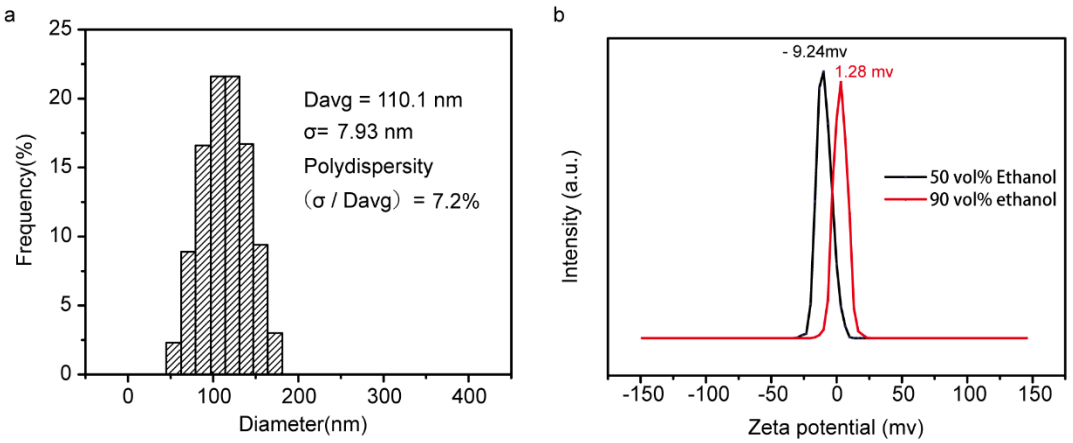

Figure S3. Particle characterization. a) The corresponding size distribution that obtained by particle size analyzer. b) Zeta potential under different solvent composition (ethanol/water). With low ethanol content, the NPs surface is negatively charged. In 90 vol% ethanol solution sample, zeta potential is around zero, indicating that the electrostatic repulsion between the particles becomes smaller, which facilitates the NPs assembly.

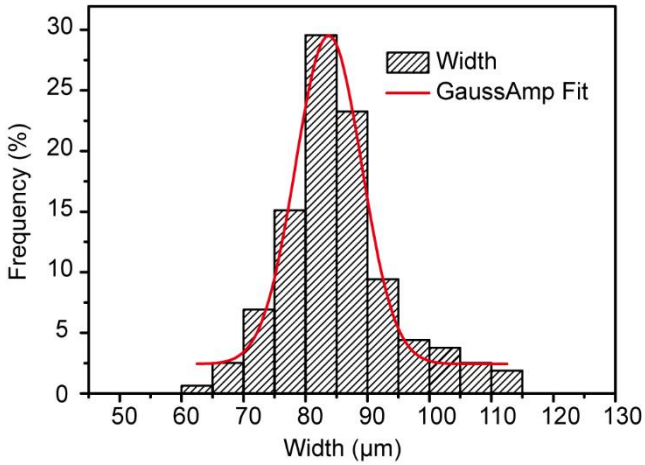

Figure S4. Corresponding rod width histogram attained by statistical analysis of over 150 rods. The width of rods is concentrated, conforms to Gaussian distribution. The samples were obtained from the suspension with 0.4 % NPs concentration and 90 vol% EtOH concentration evaporates in the vial with the vial radius of 0.9 cm. The liquid level descents with an estimated value of $1.0\ \mu m/s$.

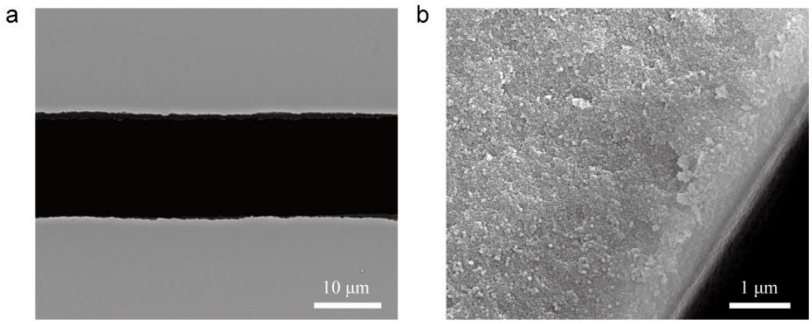

Figure S5 Typical SEM images of cracks from different view. a) Top view; b) Side view.

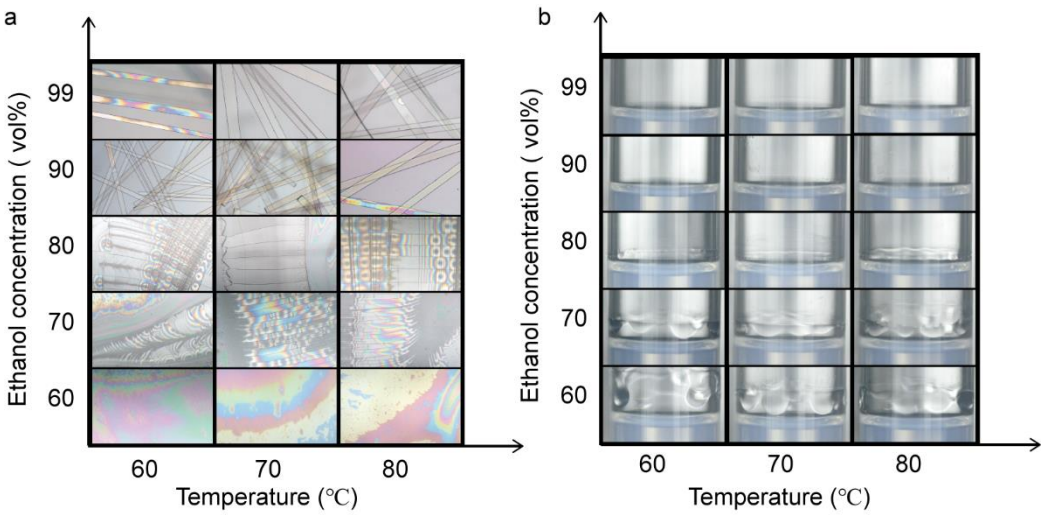

Figure S6. Effect of ethanol volume fraction on rod morphologies. a) Optical images of rod morphologies under different ethanol volume fraction. b) Direct observation of the drying process (Movie S2, Supporting information) under different ethanol concentration. Uniform cracks appear only when the ethanol concentration is higher than 90 vol%. In the case of low ethanol concentration (<90 vol%), the crack patterns are irregular or even not generated.

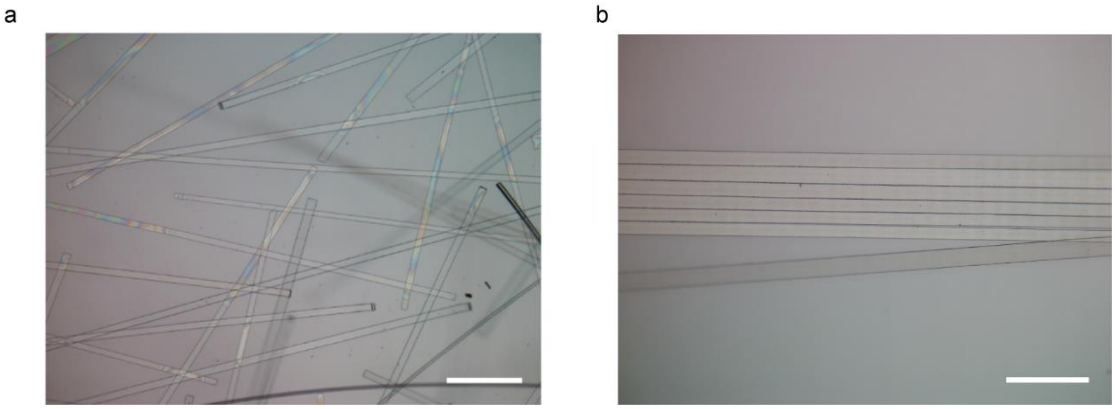

Figure S7. Representative optical images of colloidal rods prepared under different NPs concentration: (a) 0.2%, (b) 0.6%. The scale bars are 500 μm.

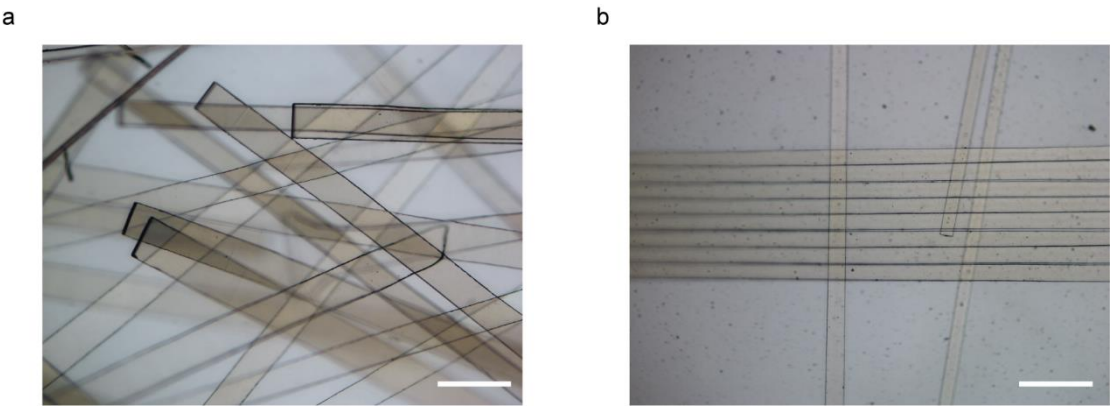

Figure S8. Representative optical images of colloidal rods prepared under different liquid descending rate: (a) 1.0 μm/s, (b) 5.0 μm/s. The scale bars are 500 μm.

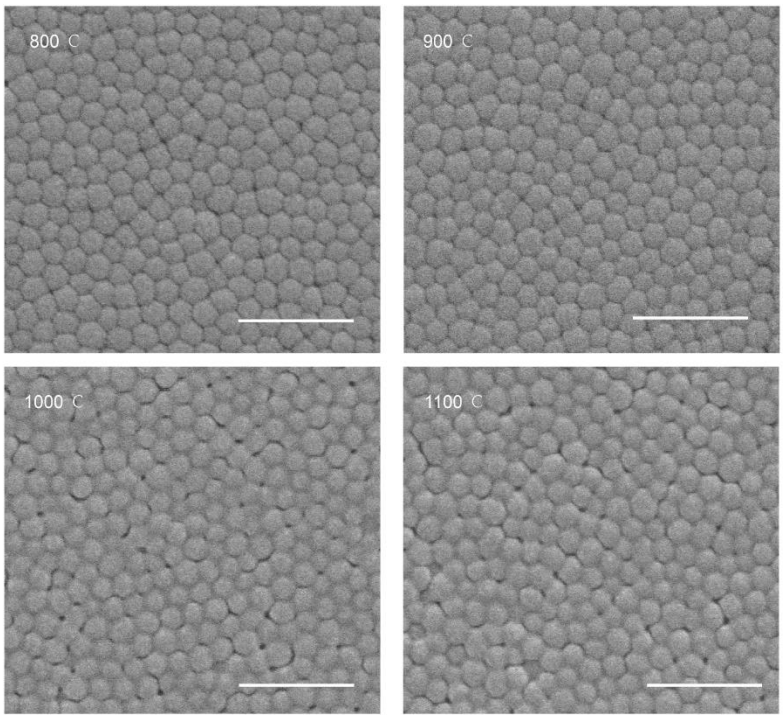

Figure S9. SEM images of rod morphologies under different annealing temperature. All the scale bars are 500 nm.

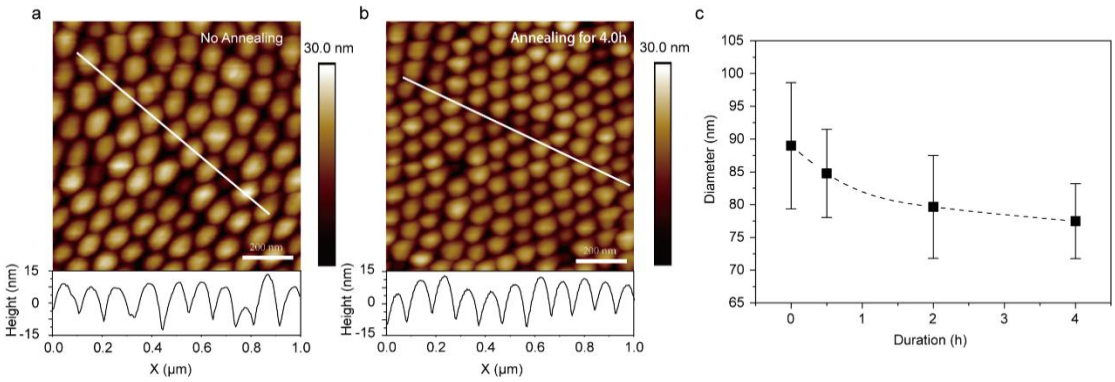

Figure S10. The effect of annealing on NPs size. a) An AFM image of the untreated rod. b) An AFM image of the rod annealed for 4 hours. c) NP diameter as a function of the annealing duration. The average diameter of NPs are 89 nm (No heat treatment), 85 nm (Annealed for 0.5 hour), 80 nm (Annealed for 2 hours), 77 nm (Annealed for 4 hours), respectively. The annealing temperature is 900 ℃.

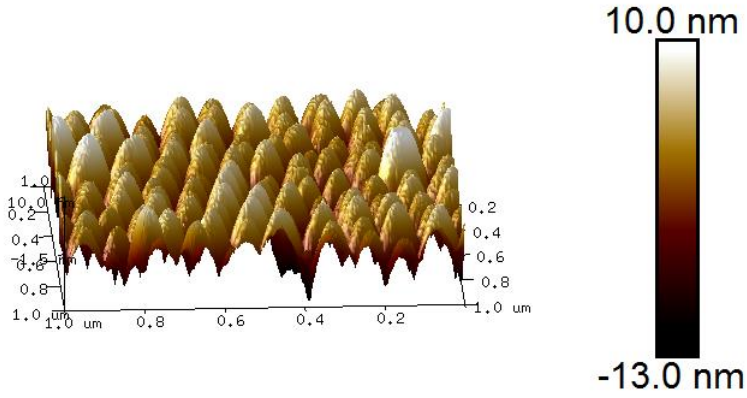

Figure S11. An AFM image shows that rods has a rough nanostructured surface, which is a positive factor for the SERS enhancement.

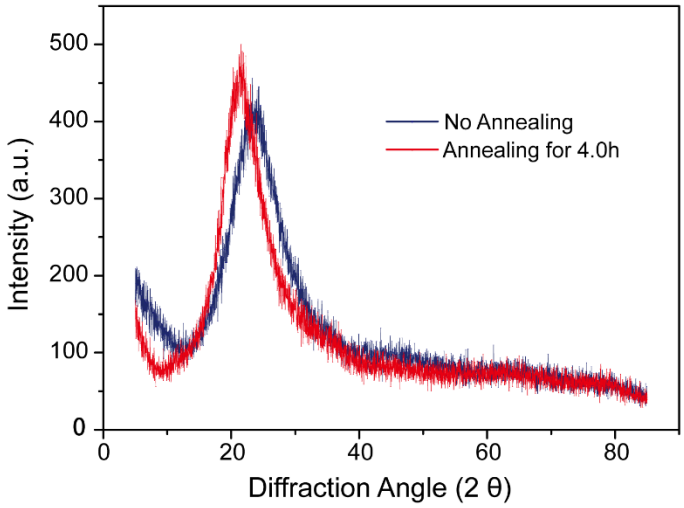

Figure S12. Wide angle X-ray diffraction of silica rods before and after 4 hours of annealing. The whole rod is polycrystalline in nature. The annealing made the diffraction peak shifted from 24° to 21°, which is representive for cristobalite structure.

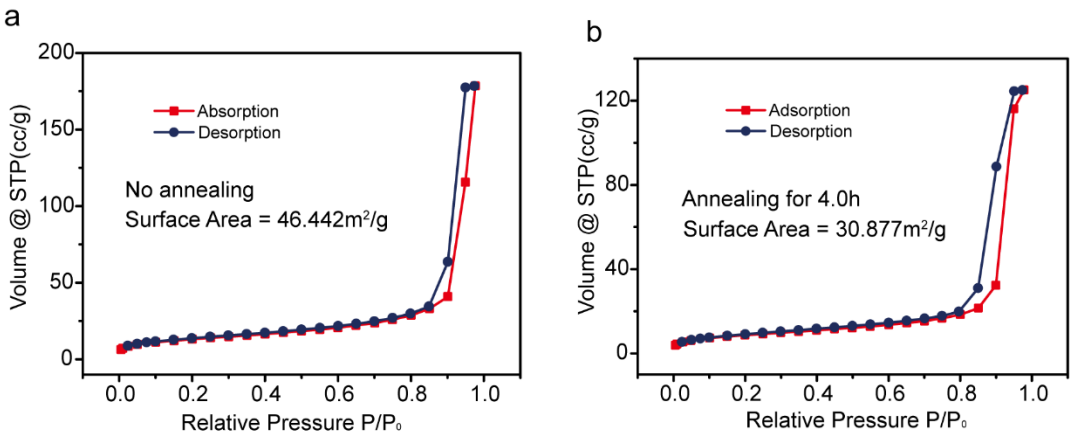

Figure S13. N_2 adsorption isotherms for silica rod before and after annealing. Due to the bridging effect of silica NPs during annealing, the surface area decreased from 46 to 30 m^2/g.

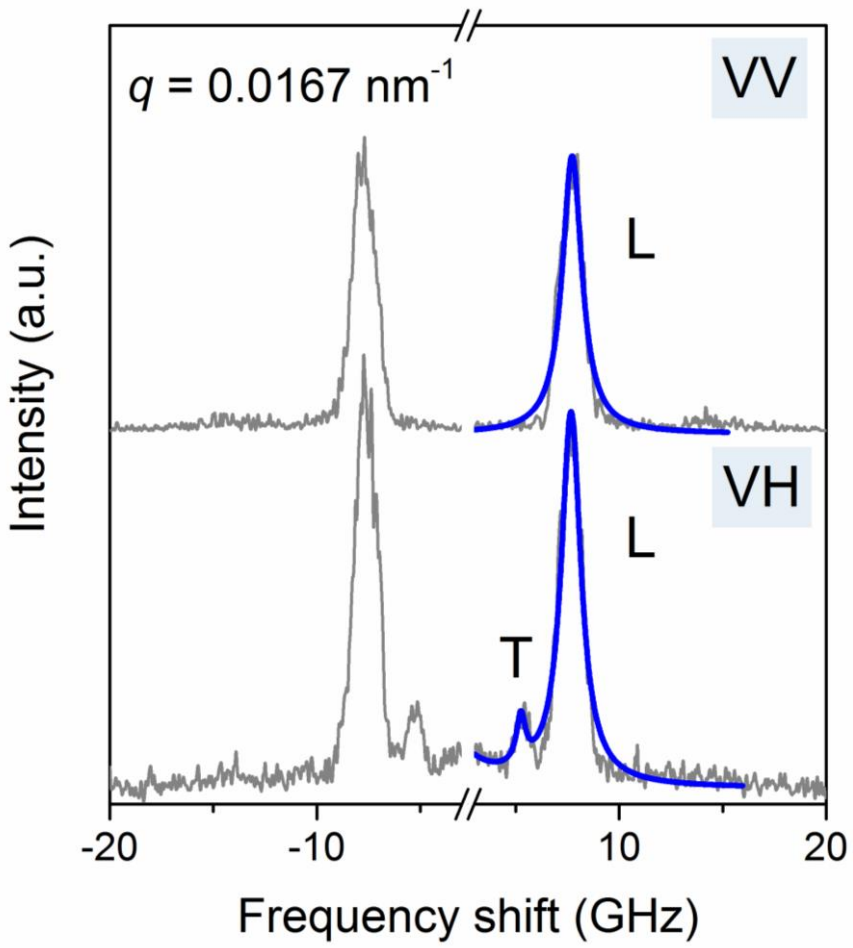

Figure S14. VV and VH BLS spectra of CRs annealed for 0.5h at q=0.00167 nm^{-1}. The experimental spectra (grey lines) are represented by Lorentzian shapes (blue lines) along with the longitudinal (L) and transverse (T) modes assignment as indicated.